PROCEEDINGS OF SCIENCE

Nucleon Vector and Axial-Vector Form Factors

Yong-Chull Jang*, **Tanmoy Bhattacharya, Rajan Gupta**
Theoretical Division, T-2, Los Alamos National Laboratory, Los Alamos, NM, 87545, U.S.A.
E-mail: ypj@lanl.gov

Boram Yoon
Computer, Computational, and Statistical Sciences, CCS-7, Los Alamos National Laboratory, Los Alamos, NM, 87545, U.S.A.

Huey-Wen Lin

Department of Physics and Astronomy, Michigan State University, MI, 48824, U.S.A

PNDME Collaboration †

We present a status report on the calculation of the isovector axial-vector and vector form factors of the nucleon using (i) eight ensembles of $N_f = 2+1+1$ HISQ fermions at lattice spacings $a = 0.12, 0.09$, and 0.06 fm and three values of light quark masses corresponding to $M_\pi = 310, 220, 130$ MeV generated by the MILC collaboration and (ii) four ensembles of clover fermions generated by the JLAB/W&M collaboration. In both cases, the clover action is used for valence quarks. Analysis of the Q^2 dependence of the form factors is carried out using the $z-$expansion and the dipole ansatz. The results for the charge radii and dipole masses are compared and found to be consistent between the two fit ansatz and between the two lattice formulations.

34th annual International Symposium on Lattice Field Theory
24-30 July 2016
University of Southampton, UK

*Speaker.

†The calculation of the form factors on the 2+1-clover ensembles is being done in collaboration with Balint Joo, Kostas Orginos, David Richards and Frank Winter.

PoS(LATTICE2016)178

1. Introduction

The isovector vector and axial-vector form factors of the nucleon are measured in a number of experiments and important properties such as the electric (r_E) and magnetic (r_M) charge radii of the proton have been extracted from electron scattering and [muonic] hydrogen spectrum. At present, there is a roughly 7σ difference between $r_E = 0.8751(61)$ fm from the CODATA world average using electron scattering data [1] and $r_E = 0.84087(39)$ fm from Lamb shift in muonic hydrogen [2, 3]. The proton magnetic radius is $r_M = 0.86^{+0.02}_{-0.03}$ fm [4]; the magnetic moment is $\mu^p = 2.792847356(23)$ for proton and $\mu^n = 1.9130427(5)$ for neutron [5]. The axial charge radius is $r_A = 0.80^{+0.07}_{-0.17} \pm 0.12$ fm (neutrino scattering) [6], $r_A = 0.74^{+0.12}_{-0.09} \pm 0.05$ fm (electroproduction) [6], $r_A = 0.68(16)$ fm (deuterium target) [7]. The goal of lattice calculations is to reach this level of precision and help resolve the various discrepencies.

The axial form-factors of nucleons are important input in the calculation of the cross-section of neutrinos on nuclear targets. These energy dependent cross-sections are needed to determine the neutrino flux, a major systematic in neutrino oscillation experiments. There is, at present, a 3σ tension between different phenomenological estimates of the effective axial mass extracted using the dipole approximation to fit the data (see Ref. [7]).

Lack of total control over systematics in vector and axial-vector form factors afflict both experimental analyses and lattice calculations. The goal is to continuously increase the precision of both experiments and lattice calculations to establish agreement or to invesigate beyond the standard model contributions in case of disagreement. In this talk we summarize the status of lattice calculations using two lattice formulations: 8 ensembles with clover-on-HISQ analysis and 4 ensembles of clover-on-clover. The lattice parameters of these ensembles are described in Refs. [8, 9, 10].

2. Nucleon Form Factors

The matrix element of the vector current within the nucleon state can be decomposed in terms of the Dirac, F_1, and Pauli, F_2, form factors as:

$$\left\langle N(\boldsymbol{p}_f)|V_\mu(\boldsymbol{Q})|N(\boldsymbol{p}_i)\right\rangle = \overline{u}_N(\boldsymbol{p}_f)\left[\gamma_\mu F_1(Q^2) + \sigma_{\mu\nu}Q_\mu\frac{F_2(Q^2)}{2m_N}\right]u_N(\boldsymbol{p}_i)\,, \tag{2.1}$$

where the four-momentum transfer $Q_\mu \equiv (p_f - p_i)_\mu$ and $Q^2 = \boldsymbol{p}_i^2 - (m_N - E_i)^2$. The momentum $\boldsymbol{p}_f \equiv 0$ since we insert a zero-momentum nucleon state at the sink timeslice. The experimental differential cross section is commonly written in terms of the Sachs electric, G_E, and magnetic, G_M, form factors defined as [11]:

$$G_E(Q^2) = F_1(Q^2) - \frac{Q^2}{4m_N^2}F_2(Q^2)\,, \qquad G_M(Q^2) = F_1(Q^2) + F_2(Q^2)\,. \tag{2.2}$$

The axial form factor, G_A, and the induced pseudoscalar form factor, G_P, are obtained from the matrix element of the axial-vector current within the nucleon state:

$$\left\langle N(\boldsymbol{p}_f)|A_\mu(\boldsymbol{Q})|N(\boldsymbol{p}_i)\right\rangle = \overline{u}_N(\boldsymbol{p}_f)\left[\gamma_\mu G_A(Q^2) + Q_\mu\frac{G_P(Q^2)}{2m_N}\right]\gamma_5 u_N(\boldsymbol{p}_i) \tag{2.3}$$

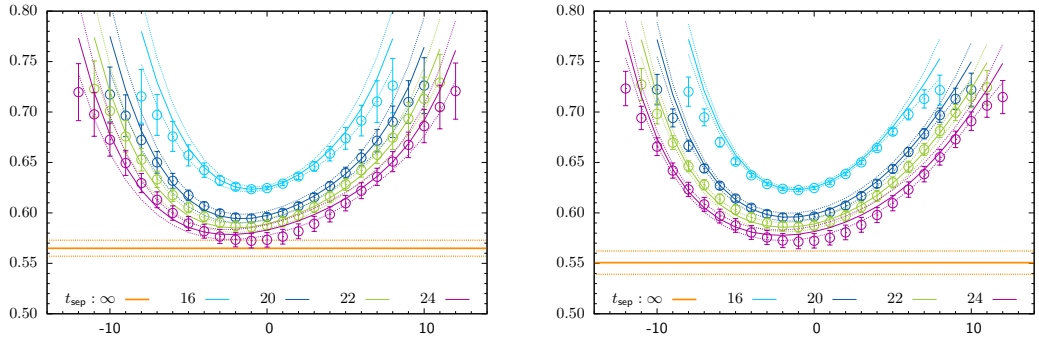

(a) 2-state (b) 4-state

Figure 1: Data for the 3-point correlator ratio, Eq. (3.3), from the a06m220 HISQ ensemble with V_4 operator insertion at lattice momenta $(1,1,1)$. $G_E(Q^2)$ are extracted from such data.

On the lattice, one first calculates nucleon 3-point functions with vector and axial-vector operator insertion for a large set of momentum transfer Q_μ. From these 3-point functions, we extract matrix elements as described in [9, 10]. Various form factors are obtained from linear combinations of these matrix elements using appropriate Dirac matrices γ_μ and values of momentum insertion Q_μ.

3. Controlling the Excited-State Contamination (ESC)

High statistics estimates were obtained cost-effectively by using the truncated solver method with bias correction (AMA) [12, 13], and the coherent source sequential propagator method [9, 10]. The tuning of the covariant gaussian source smearing size σ and the values of the source-sink separations $t_{\rm sep}$ used in the simulations are described in Refs. [9, 10]. Results presented here are obtained using amplitudes $\mathscr{A}_i$ and energies E_i from 4-state fits to 2-point correlators, stablized using non-trivial priors as described in Ref. [10, 8]:

$$C^{(2\rm pt)}(t,\boldsymbol{p}) = |\mathscr{A}_0|^2 e^{-E_0 t} + |\mathscr{A}_1|^2 e^{-E_1 t} + |\mathscr{A}_2|^2 e^{-E_2 t} + |\mathscr{A}_3|^2 e^{-E_3 t}\,. \tag{3.1}$$

These $\mathscr{A}_i$ and E_i are used as inputs in 2-state fits to 3-point data at multiple $t_{\rm sep}$ and τ to extract the matrix element $\langle 0'|\mathscr{O}_\Gamma|0\rangle$ in the $t_{\rm sep}\to\infty$ limit:

$$\begin{aligned} C_\Gamma^{(3\rm pt)}(t;\tau;\boldsymbol{p}',\boldsymbol{p}) = {} & |\mathscr{A}_0'||\mathscr{A}_0|\langle 0'|\mathscr{O}_\Gamma|0\rangle e^{-E_0 t - M_0(\tau-t)} + |\mathscr{A}_1'||\mathscr{A}_1|\langle 1'|\mathscr{O}_\Gamma|1\rangle e^{-E_1 t - M_1(\tau-t)} \\ & + |\mathscr{A}_0'||\mathscr{A}_1|\langle 0'|\mathscr{O}_\Gamma|1\rangle e^{-E_0 t - M_1(\tau-t)} + |\mathscr{A}_1'||\mathscr{A}_0|\langle 1'|\mathscr{O}_\Gamma|0\rangle e^{-E_1 t - M_0(\tau-t)}\,. \end{aligned} \tag{3.2}$$

To estimate errors, these two fits are done within a single Jackknife process with the χ^2/d.o.f. for each fit minimized using the full covariance matrix. The charges G_A and G_E used for normalizing the form factors are taken from 3-state fits to the 3-point correlators [10, 8].

In Fig. 1, we illustrate ESC in 3-point functions by plotting the ratio, Eq. (3.3), with the insertion of the V_4 operator at lattice momentum $(1,1,1)$. Dependence on $t_{\rm sep}$ and τ indicates ESC. We control this by making combined fits versus $t_{\rm sep}$ and τ using Eq. 3.2. The input amplitudes and energies, $\mathscr{A}_i$ and E_i, are from 2-state (Fig. 1a) and 4-state (Fig. 1b) fits to Eq. (3.1).

$$\frac{C_\Gamma^{(3\rm pt)}(t,\tau;\boldsymbol{p}',\boldsymbol{p})}{C^{(2\rm pt)}(\tau,\boldsymbol{p}')} \left[\frac{C^{(2\rm pt)}(t,\boldsymbol{p}')C^{(2\rm pt)}(\tau,\boldsymbol{p}')C^{(2\rm pt)}(\tau-t,\boldsymbol{p})}{C^{(2\rm pt)}(t,\boldsymbol{p})C^{(2\rm pt)}(\tau,\boldsymbol{p})C^{(2\rm pt)}(\tau-t,\boldsymbol{p}')}\right]^{1/2}\,. \tag{3.3}$$

Ensemble	Fit	r_E [fm]	χ^2/DOF	r_M [fm]	μ	χ^2/DOF	r_A [fm]	χ^2/DOF
a12m310AMA	D	0.729(021)	1.026	0.643(028)	4.234(057)	0.664	0.473(022)	1.150
	z^2	0.742(007)	1.630	0.694(015)	4.370(078)	0.448	0.494(011)	0.709
	z^3	0.731(015)	2.132	0.641(109)	4.250(241)	0.620	0.481(026)	0.896
a12m220LAMA	D	0.764(034)	0.234	0.683(068)	4.252(098)	0.721	0.498(053)	0.392
	z^2	0.791(016)	0.130	0.750(039)	4.370(130)	0.198	0.511(023)	0.423
	z^3	0.791(049)	0.194	0.811(115)	4.439(184)	0.118	0.517(038)	0.613
a09m310	D	0.677(056)	1.005	0.648(103)	4.146(131)	0.487	0.487(091)	0.263
	z^2	0.692(021)	1.255	0.683(034)	4.227(161)	0.884	0.496(030)	0.353
	z^3	0.718(053)	1.755	0.359(424)	3.705(432)	0.070	0.479(049)	0.432
a09m220	D	0.719(083)	0.318	0.674(126)	4.046(148)	0.941	0.492(116)	1.169
	z^2	0.730(037)	0.538	0.728(074)	4.105(193)	1.651	0.524(057)	1.564
	z^3	0.613(140)	0.344	-	-	-	0.613(079)	1.476
a09m130AMA	D	0.914(076)	7.356	0.712(098)	3.483(086)	1.798	0.594(100)	6.206
	z^2	1.101(044)	5.061	0.258(446)	3.301(129)	1.388	0.664(040)	8.146
	z^3	1.341(068)	0.250	1.338(365)	3.874(399)	0.474	0.937(076)	6.769
a06m310AMA	D	0.708(074)	0.692	0.648(092)	3.987(100)	0.974	0.495(094)	0.782
	z^2	0.712(023)	0.763	0.652(029)	3.954(109)	0.014	0.496(027)	0.240
	z^3	0.755(038)	0.218	0.643(155)	3.935(341)	0.024	0.493(039)	0.354
a06m220AMA	D	0.741(039)	2.165	0.643(053)	3.821(063)	0.706	0.484(046)	0.788
	z^2	0.778(016)	1.227	0.695(035)	3.891(090)	0.728	0.492(020)	0.925
	z^3	0.812(028)	0.834	0.856(153)	4.128(275)	0.628	0.519(038)	1.037
a06m130AMA	D	0.752(073)	0.899	0.667(091)	3.916(132)	0.678	0.464(079)	0.719
	z^2	0.817(057)	0.887	0.641(150)	3.915(200)	0.787	0.395(083)	0.777
	z^3	0.820(116)	1.034	0.560(744)	3.873(400)	0.940	0.378(197)	0.904

Table 1: Charge radii from the Clover-on-HISQ analysis

4. The Nucleon Charge Radii

The mean squared charge radii r_i ($i \in$ electric (E), magnetic (M) and axial (A)), are defined by the slope of the form factor with respect to the momentum transfer Q^2 at $Q^2 = 0$:

$$\langle r_i^2 \rangle \equiv -6 \frac{d}{dQ^2} \left(\hat{G}_i(Q^2)/\hat{G}_i(0) \right)\big|_{Q^2=0} . \tag{4.1}$$

We use the normalized $\hat{G}_{E,M} = G_{E,M}/g_E$ and $\hat{G}_{A,P} = G_{A,P}/g_A$ with g_E the electric charge and g_A the axial charge. $\hat{G}_{E,M}(Q^2)$ and $\hat{G}_A(Q^2)$ are commonly parameterized using the dipole ansatz,

$$\hat{G}_i(Q^2) = \hat{G}_i(0)/\left(1 + Q^2/\mathscr{M}_i^2\right)^2 , \tag{4.2}$$

where $\mathscr{M}_i$ is the dipole mass, in terms of which the charge radii are $\langle r_i^2 \rangle = 12/\mathscr{M}_i^2$. By construction $\hat{G}_{E,A}(0) = 1$ and the anomalous magnetic moment κ is $\hat{G}_M(0) = \mu \equiv 1 + \kappa$. The dipole fits for G_E, G_M, and G_A are shown in Figs. 2 and 3 and estimates of the radii in Tables 1 and 2.

Experimental data are often analyzed using the Kelly parameterization [14]:

$$\hat{G}_X(Q^2) = \hat{G}(0) \sum_{k=0}^{n} a_k \tau^k / \left\{ 1 + \sum_{k=1}^{n+2} b_k \tau^k \right\} , \quad \hat{G}_Y(Q^2) = \frac{A\tau}{1 + B\tau} \frac{1}{\left(1 + Q^2/0.71\text{GeV}^2\right)^2} , \tag{4.3}$$

where $\tau = Q^2/4\mathscr{M}^2$. The parameters $\mathscr{M}$, $G(0)$, a_k, b_k, A, and B are determined from fit to the data. The parameterization $\hat{G}_X(Q^2)$ is used for the electic and magentic form factors for the proton and

Ensemble	Fit	r_E [fm]	χ^2/DOF	r_M [fm]	μ	χ^2/DOF	r_A [fm]	χ^2/DOF
a114m315 (S_5S_5)	D	0.770(030)	0.417	0.667(033)	4.384(043)	0.239	0.488(028)	0.882
	z^2	0.769(009)	0.544	0.690(010)	4.428(044)	0.346	0.501(009)	0.559
	z^3	0.781(012)	0.227	0.680(019)	4.408(054)	0.335	0.500(012)	0.652
a081m315 (S_5S_5)	D	0.715(057)	0.871	0.616(086)	4.168(136)	1.366	0.439(075)	1.325
	z^2	0.717(017)	0.909	0.690(018)	4.432(131)	2.037	0.482(021)	2.195
	z^3	0.702(041)	1.031	0.479(107)	3.876(229)	0.704	0.412(037)	1.329
a081m315 (S_7S_7)	D	0.704(039)	0.577	0.596(067)	4.201(108)	1.044	0.445(081)	0.749
	z^2	0.716(010)	0.443	0.677(021)	4.460(127)	1.270	0.480(024)	1.053
	z^3	0.689(023)	0.238	0.600(082)	4.228(244)	1.275	0.438(035)	0.582
a081m315 (S_9S_9)	D	0.703(022)	1.874	0.593(035)	4.108(087)	1.459	0.424(026)	2.059
	z^2	0.709(006)	0.656	0.671(013)	4.368(106)	0.831	0.462(011)	1.255
	z^3	0.716(019)	0.741	0.658(064)	4.327(220)	0.987	0.466(023)	1.454
a079m195 (S_7S_7)	D	0.726(039)	0.648	0.638(044)	4.105(079)	1.064	0.453(037)	0.417
	z^2	0.767(018)	0.621	0.705(043)	4.195(120)	1.396	0.453(023)	0.519
	z^3	0.746(030)	0.600	0.472(275)	3.949(243)	1.404	0.423(042)	0.466
a079m195L (S_7S_7)	D	0.750(050)	1.379	0.707(068)	4.514(119)	0.485	0.546(078)	0.473
	z^2	0.780(033)	1.645	0.753(037)	4.555(130)	0.866	0.566(032)	0.503
	z^3	0.743(055)	1.788	0.587(142)	4.404(165)	0.594	0.577(048)	0.572

Table 2: Charge radii from the Clover-on-Clover analysis

Ensemble	$\mathcal{M}_E$ [GeV]	$\mathcal{M}_M$ [GeV]	$\mathcal{M}_A$ [GeV]
a12m310AMA	0.938(008)	1.062(013)	1.444(020)
a12m220LAMA	0.895(012)	1.002(029)	1.372(042)
a09m310	1.010(024)	1.055(048)	1.405(076)
a09m220	0.950(032)	1.014(055)	1.388(094)
a09m130AMA	0.748(018)	0.961(038)	1.151(056)
a06m310AMA	0.965(029)	1.055(043)	1.380(075)
a06m220AMA	0.923(014)	1.063(025)	1.413(039)
a06m130AMA	0.909(025)	1.025(040)	1.475(073)

(a) dipole masses from the Clover-on-HISQ analysis

Ensemble	$\mathcal{M}_E$ [GeV]	$\mathcal{M}_M$ [GeV]	$\mathcal{M}_A$ [GeV]
a114m315 (S_5S_5)	0.888(010)	1.025(015)	1.402(023)
a081m315 (S_5S_5)	0.956(022)	1.110(045)	1.556(077)
a081m315 (S_7S_7)	0.971(016)	1.148(037)	1.534(081)
a081m315 (S_9S_9)	0.973(009)	1.152(020)	1.612(029)
a079m195 (S_7S_7)	0.941(015)	1.072(021)	1.508(035)
a079m195L (S_7S_7)	0.912(018)	0.967(027)	1.252(052)

(b) dipole masses from the Clover-on-Clover analysis

Table 3: Estimates of dipole mass

the magnetic form factor for the neutron, while the electric form factor for the neutron is fit using G_Y. The lattice data are compared against Kelly fits to experimental data in Fig. 2. For the Kelly fits shown in Fig. 2, we used the parameters given in Table I in Ref. [14].

A model independent approach, incorporating analyticity of QCD, is the z-expansion [15, 6]:

$$\hat{G}(Q^2) = \sum_{k=0}^{\infty} a_k z(Q^2)^k \qquad \text{with} \qquad z = \frac{\sqrt{t_{\rm cut}+Q^2} - \sqrt{t_{\rm cut}+Q_0^2}}{\sqrt{t_{\rm cut}+Q^2} + \sqrt{t_{\rm cut}+Q_0^2}}\,. \tag{4.4}$$

The a_k are fit parameters. Using $t_{\rm cut} = 4m_\pi^2$, position of the branch cut for the electric form factor [15] and $t_{\rm cut} = 9m_\pi^2$ for the axial form factor [6], the domain of analyticity in z is the unit circle. We set the free parameter $Q_0 = 0$, and for m_π use the pion with sea quark mass for each ensemble. For the magnetic form factor, we use the same $t_{\rm cut}$ as for the electic form factor. Results for the radii r_i, using a quadratic and cubic $z-$expansion, are also given in Tables 1 and 2.

Lastly, we compare in Figs. 3c and 3d the lattice data for the pseudoscalar form factor $\hat{G}_P$

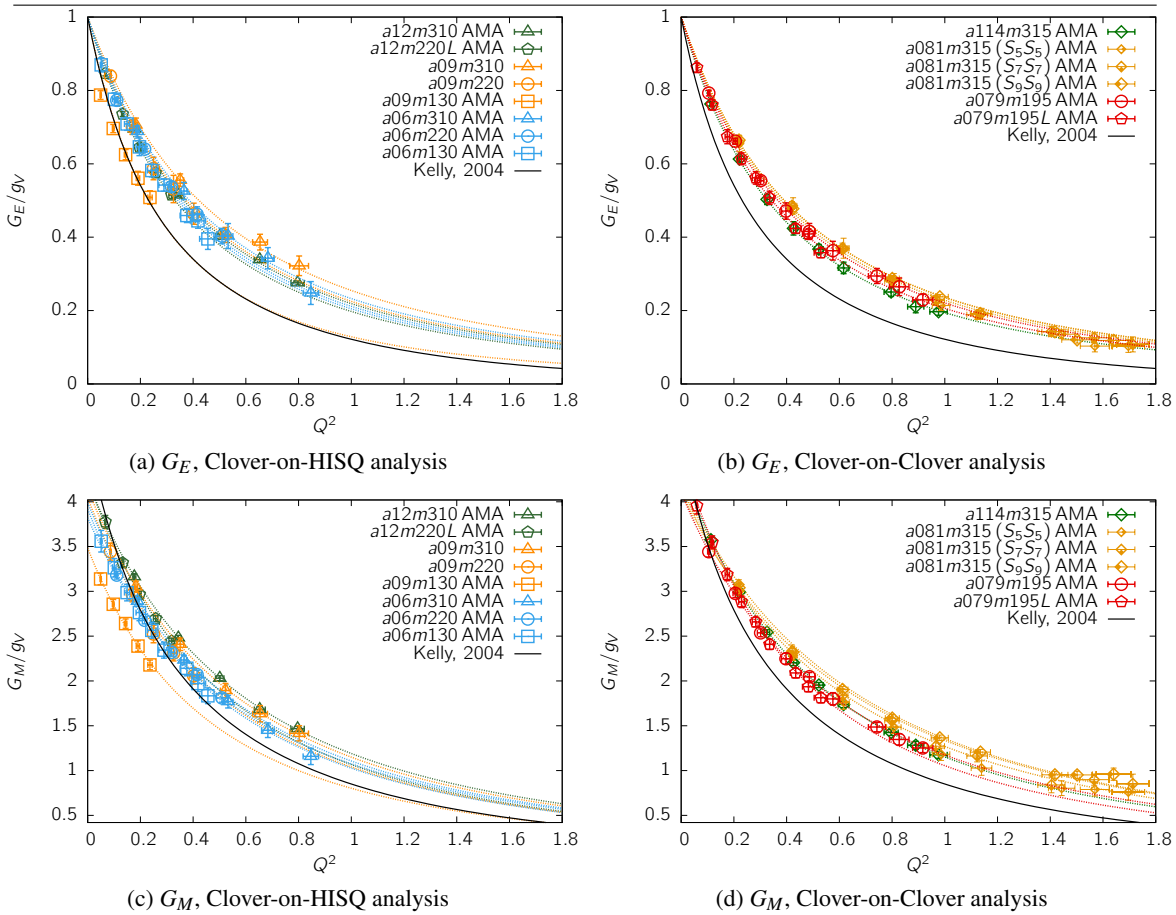

(a) G_E, Clover-on-HISQ analysis

(b) G_E, Clover-on-Clover analysis

(c) G_M, Clover-on-HISQ analysis

(d) G_M, Clover-on-Clover analysis

Figure 2: Data for $G_E(Q^2)$ and $G_M(Q^2)$ and dipole and Kelly fits to them.

against the pion-pole dominance ansatz (product of the axial form factor times a pion pole):

$$\hat{G}_P(Q^2) = \hat{G}_A(Q^2) \left[\frac{4m_p^2}{Q^2 + m_\pi^2} \right], \tag{4.5}$$

where we use $m_p = 939$ MeV for the proton mass and $m_\pi = 135$ MeV for the pion mass.

5. Conclusions

Some concluding observations are: (i) the dipole ansatz works well except on the a09m130 HISQ ensemble. (ii) Estimates of r_i agree between the dipole and fits quadratic and cubic in z. (iii) The r_i are slightly larger (i.e. $\mathscr{M}_i$ slightly smaller) from comparable clover-on-clover versus clover-on-HISQ ensembles. (iv) In both lattice formulations, variations in r_i versus m_π for fixed lattice spacing a, and versus a for fixed m_π are small. A detailed analysis is underway.

Acknowledgements: We thank the MILC Collaboration for the 2+1+1-flavor HISQ ensembles and JLab/W&M collaboration for the 2+1 clover lattices. Simulations were carried out on computer facilities of (i) Oak Ridge Leadership Computing Facility; (ii) the USQCD Collaboration; (iii) the National Energy Research Scientific Computing Center and (iv) Institutional Computing at Los Alamos National Lab. Work supported by the DOE and Los Alamos LDRD.

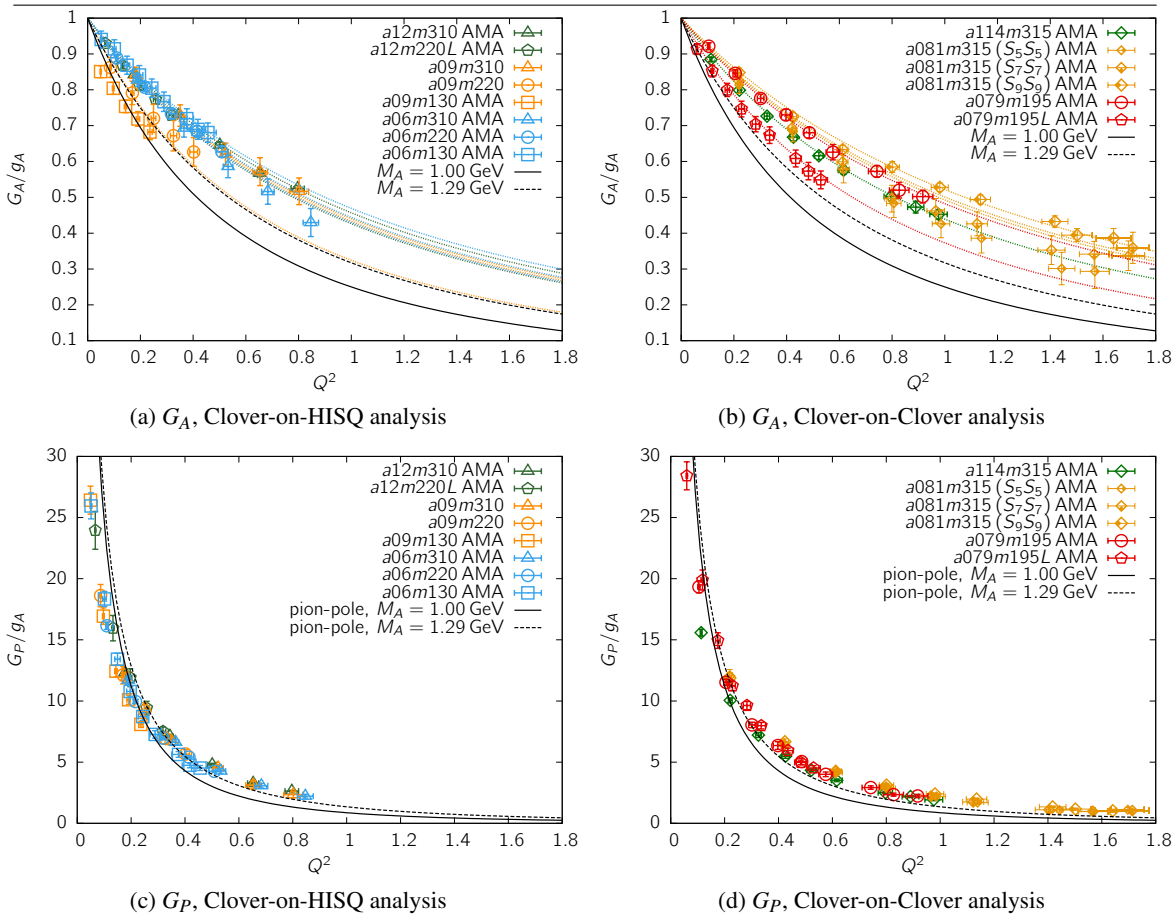

(a) G_A, Clover-on-HISQ analysis

(b) G_A, Clover-on-Clover analysis

(c) G_P, Clover-on-HISQ analysis

(d) G_P, Clover-on-Clover analysis

Figure 3: Data for $G_A(Q^2)$ and $G_P(Q^2)$ with dipole fits to $G_A(Q^2)$, pion-pole dominance to $G_P(Q^2)$.

References

[1] P. J. Mohr *et al.*, CODATA group, *Rev. Mod. Phys.* **88** (2016), no. 3 035009, [1507.07956].

[2] A. Antognini *et al.*, *EPJ Web Conf.* **113** (2016) 01006, [1509.03235].

[3] R. Pohl1 *et al.*, CREMA, *Science* **353** (2016), no. 6300 669–673.

[4] I. T. Lorenz, H. W. Hammer, and U.-G. Meissner, *Eur. Phys. J.* **A48** (2012) 151, [1205.6628].

[5] K. A. Olive *et al.*, Particle Data Group, *Chin. Phys.* **C38** (2014) 090001.

[6] B. Bhattacharya, R. J. Hill, and G. Paz, *Phys. Rev.* **D84** (2011) 073006, [1108.0423].

[7] A. S. Meyer *et al.*, *Phys. Rev.* **D93** (2016), no. 11 113015, [1603.03048].

[8] R. Gupta *et al.*, *PoS* **LATTICE2016** (2016) 157.

[9] T. Bhattacharya *et al.*, *Phys. Rev.* **D94** (2016), no. 5 054508, [1606.07049].

[10] B. Yoon *et al.*, 1611.07452.

[11] R. G. Sachs, *Phys. Rev.* **126** (1962) 2256–2260.

[12] G. S. Bali *et al.*, *Comput. Phys. Commun.* **181** (2010) 1570–1583, [0910.3970].

[13] T. Blum, T. Izubuchi, and E. Shintani, *Phys. Rev.* **D88** (2013), no. 9 094503, [1208.4349].

[14] J. J. Kelly, *Phys. Rev.* **C70** (2004) 068202.

[15] R. J. Hill and G. Paz, *Phys. Rev.* **D82** (2010) 113005, [1008.4619].